



# Gradient-distributed $\text{NiCo}_2\text{O}_4$ nanorod electrode for redox flow batteries: Establishing the ordered reaction interface to meet the anisotropic mass transport

Rui Wang<sup>a</sup>, Mingsheng Hao<sup>b</sup>, Chao He<sup>c</sup>, Zhengjun Tu<sup>c</sup>, Fazheng Chong<sup>b</sup>, Yinshi Li<sup>b,c,\*</sup>

<sup>a</sup> School of Chemical Engineering and Technology, Xi'an Jiaotong University, Xi'an, Shaanxi 710049, China

<sup>b</sup> Key Laboratory of Thermo-Fluid Science and Engineering of Ministry of Education, School of Energy and Power Engineering, Xi'an Jiaotong University, Xi'an, Shaanxi 710049, China

<sup>c</sup> School of Future Technology, Xi'an Jiaotong University, Xi'an, Shaanxi 710049, China

## ARTICLE INFO

### Keywords:

Flow battery  
Porous electrode  
Ordered reaction  
Mass transport  
 $\text{NiCo}_2\text{O}_4$  nanorod

## ABSTRACT

In this work, a gradient-distributed  $\text{NiCo}_2\text{O}_4$  nanorod-composed graphite felt electrode (G- $\text{NiCo}_2\text{O}_4$ -GF) was proposed and developed to achieve an ordered reaction toward the nonuniform mass transport in flow batteries. To this end, the ordered-nucleation hydrothermal method was designed, for which the  $\text{NiCo}_2\text{O}_4$  nanorod was grown concentrated in one side of electrode, and gradually decreased along the through-plane direction until hardly any in the other side. Theoretical calculating results indicated that the G- $\text{NiCo}_2\text{O}_4$ -GF electrode yielded an obviously lower difference of local current density along through-plane direction, nearly one third of the uniformly-enhanced electrode. Flow battery assembled with the as-prepared electrode exhibited high energy efficiency (88.81 % at  $100 \text{ mA cm}^{-2}$ ), superior operation current density ( $500 \text{ mA cm}^{-2}$ ), and long cycling stability (162 h, 200 cycles). This work provides an effective approach to develop the high-performance electrode for flow batteries.

## 1. Introduction

Developing advanced large-scale energy storage systems (ESSs) is in urgent need to satisfy the worldwide energy demand of utilizing renewable energies, such as wind and solar [1–3]. In the power grid, instability and intermittency of renewable energy power output must be effectively counterbalanced by the ESSs to insure a stable and safe power supply continuous or as-needed. In this regard, the flow batteries (FBs), with the advantages of decoupled capacity-power characteristics, favorable safety, long lifetime, superior flexibility and environmental friendliness, are deemed as one of the most promising large-scale ESS technologies [4]. Among various flow batteries, the vanadium flow batteries (VFBs), that cycling V-based active species in both half-cell to intrinsically minimize cross-contamination, possesses the most advantageous durability and minimum reclamation cost for the optimistic commercial-prospects [5].

Although promising, there are some common problems in flow batteries, such as narrow electrochemical window limiting operating

voltage, extra pump power and high ohm drop reducing system efficiency. More noteworthy, the commercial application process of FB technologies is still impeded by the high capital cost, especially the high-cost stack materials and active reactants [6]. In order to reduce the capital cost for the increasing market requirement, one straightforward strategy is to improve the power density performance of battery while remain high energy efficiency and high electrolyte utilization. One effective method is to collocate different common metallic redox couples to increase cell theoretical potential. Unfortunately, the polarizations in flow batteries, closely connected with redox reaction and mass transport processes, are raised with current density increase, resulting in low capacity and high overpotential [7]. As for VFB, the cell polarizations can be categorized into activation polarization, ohmic polarization and concentration polarization [8]. Therefore, to construct a high-performance VFB, the attention should be paid close to the redox reaction and mass transport processes to reduce these three kinds of polarizations synchronously.

As a crucial component in the VFB, the electrode, not merely serves

\* Corresponding author at: Key Laboratory of Thermo-Fluid Science and Engineering of Ministry of Education, School of Energy and Power Engineering, Xi'an Jiaotong University, Xi'an, Shaanxi 710049, China.

E-mail address: [ysli@mail.xjtu.edu.cn](mailto:ysli@mail.xjtu.edu.cn) (Y. Li).

<https://doi.org/10.1016/j.apcatb.2023.122773>

Received 9 January 2023; Received in revised form 13 April 2023; Accepted 15 April 2023

Available online 16 April 2023

0926-3373/© 2023 Elsevier B.V. All rights reserved.

active sites for redox reaction, but also provides the porous media for active species and ions transport, directly determining battery performance [9]. The most-used carbon-based porous electrode, such as graphite felt (GF) and carbon paper (CP), could meet the operation demand of VFB, but still emerge some issues: i) chemically-inert graphite structure and smooth fiber surface limits the activity and area for reaction, increasing the activation polarization [10]; ii) in addition to the well-known ohmic polarization in electrolytic solution, high electrode thickness enlarges the electrical resistance and ion transport distance, influencing the ohmic polarization [11]; iii) the adverse side reaction caused by potential variation (hydrogen and oxygen evolution reactions) and the porous property in electrode lead to high resistance for mass transport, increasing the concentration polarization [12].

In terms of reducing the activation polarization, various nano-materials, such as Bi [13,14], CoO [15] and TiN [16], were modified to enhance the surface activity. And some nanostructures, such as graphene [17,18], MOF [19] and Mxene [20], were decorated to enlarge the electrode area. However, the equally crucial mass transport process has been ignored in these uniform modification methods, hindering further improvement of battery performance. Typically, due to continuously-occurred reaction process, the concentration of active species is decreased along the flow direction in electrode, leading to weak reaction in local region and low utilization rate of active sites [21]. Furthermore, the ensuing high local current density easily gives rise to the membrane penetration and the electrode inactivation, presenting challenges to the economy and durability of VFBs [22]. In regard to reduce the ohmic polarization, the electrolyte flow type in cell is changed from the flow-through pattern to the flow-by pattern, so that lowering electrode thickness by circulating electrolyte in the outboard flow field [23]. Despite the wide application of this flow-by pattern in

FBs, the mismatching problem between redox reaction and mass transport is further aggravated. Zhao et al. pointed that the current density distribution is uneven along the CP electrode thickness direction in the flow-by-type VFB [24]. Our recent study also found the anisotropic characteristic of electrolyte velocity from the flow field side to membrane side, for nearly ten-times difference in two sides of GF electrode [25]. The anisotropic mass transport property in electrode decreases the local concentration of active species (simulation results seen in Figs. S2 and S3), leading to higher concentration polarization, especially at the final state of charge-discharge process. What is worse, in the high-flow-rate field side of electrode, proton transport distance is long and modified structures are easily washed out, while active surface is exposed to quite insufficient reactant in the low-flow-rate membrane side (simulation results seen in Figs. S4 and S5). The mismatching between reaction and transport in electrode further aggravate the activation polarization and the ohmic polarization of FBs. Additionally, high conductivity of porous matrix is also required to obtain uniform current distributions. Thus, the electrode for flow batteries should be built meticulously to meet both transport and reaction requirement.

As an ideal electrode for flow batteries, the active surface should match with the anisotropic mass transport properties, for that the reaction intensity can be varied along the through-plane direction to minimize the cell polarization. To realize this target, an ordered-reaction electrode, composed with gradient-distributed  $\text{NiCo}_2\text{O}_4$  nanorods, was proposed and developed in this work for the first time. Thanks to the ingeniously designed ordered-nucleation hydrothermal method, the  $\text{NiCo}_2\text{O}_4$  nanorod was grown concentrated in one side, and gradually decreased in the direction of thickness until hardly any in the other side. As shown in Fig. 1, the gradient-distributed  $\text{NiCo}_2\text{O}_4$  nanorod-composed graphite felt electrode (G- $\text{NiCo}_2\text{O}_4$ -GF) can play a providential role for

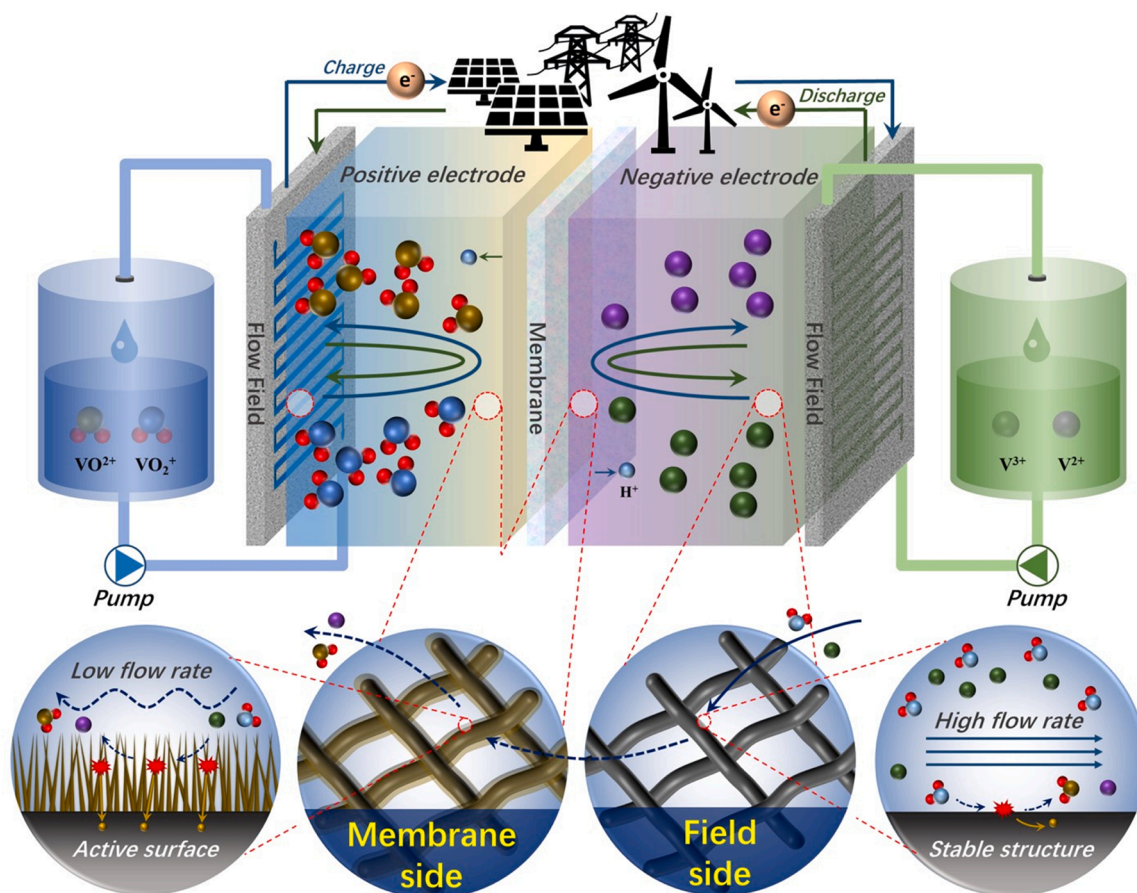


Fig. 1. Schematic of the gradient-distributed  $\text{NiCo}_2\text{O}_4$  nanorod-composed graphite felt electrode.

balancing both anisotropic transport properties and ordered reaction requirement: i) in the membrane side, the closely arranged NiCo<sub>2</sub>O<sub>4</sub> nanorods with high activity accelerate the local redox reaction and shortens the distance for proton transport, reducing cell polarization; ii) in the field side, the smooth carbon-based framework with high mechanical strength keeps the porous stable against electrolyte washing out and offers path way for mass transport, enhancing electrode stability; iii) in the whole electrode, the gradient-modification structure achieved an ordered reaction skillfully suited to the anisotropic transport properties, uniformizing current distribution and lowering overpotential of battery. The superior activity of NiCo<sub>2</sub>O<sub>4</sub> nanorod towards vanadium ion reaction was verified by electrochemical measurements. Based on experimental results, the ordered-reaction model for G-NiCo<sub>2</sub>O<sub>4</sub>-GF electrode was built by theoretical derivation and the synergic relationship between reaction and transport was further clarified via multi-physics simulation. Attributed to the ordered reaction interface, VFB assembled with G-NiCo<sub>2</sub>O<sub>4</sub>-GF electrode achieved high energy efficiency, superior operation current density, and long cycling stability.

## 2. Methods

### 2.1. Materials

Graphite felt (GF, the porosity of 95 %, thickness of 2.2 mm, specific area of 2.3 m<sup>2</sup> g<sup>-1</sup>) kindly was provided by Liaoning Jingu Carbide Co., Ltd. Nickel chloride hexahydrate (NiCl<sub>2</sub>·6 H<sub>2</sub>O), cobalt chloride hexahydrate (CoCl<sub>2</sub>·6 H<sub>2</sub>O) and urea (CH<sub>4</sub>N<sub>2</sub>O) were received from Aladdin. Vanadyl sulfate (VOSO<sub>4</sub>) was purchased from Zhongtian Chemical Ltd. Sulfuric acid (H<sub>2</sub>SO<sub>4</sub>) was purchased from Sigma-Aldrich. The Nafion NRE-212 membrane was from DuPont.

### 2.2. Preparation of G-NiCo<sub>2</sub>O<sub>4</sub>-GF

In order to enhance the hydraulic permeability conducted to nanorod nucleation, the pristine GF was firstly heated with a heating rate of 5 °C min<sup>-1</sup> at 400 °C for 4 h in air atmosphere to achieve thermally treated graphite felt (T-GF). Then, 0.2 mM NiCl<sub>2</sub>·6 H<sub>2</sub>O, 0.4 mM CoCl<sub>2</sub>·6 H<sub>2</sub>O and 1.4 mM urea was dissolved in 40 mL ultrapure water to form the low-concentration solution for the anisotropic nucleation. The mix solution was poured into 50-mL Teflon-lined stainless-steel autoclave. And the T-GF was laid flat on the bottom of the autoclave to create the condition for uneven growth of nanorod. Where after, the sealed autoclave was treated at 120 °C for 6 h to generate gradient-distributed NiCo<sub>2</sub>O<sub>4</sub> nanorod on graphite fiber. After ultrasonic treating in deionized water for 30 min and dried thoroughly, the G-NiCo<sub>2</sub>O<sub>4</sub>-GF electrode was achieved.

### 2.3. Materials characterization

The scanning electron microscope (Gemini 300, ZEISS) was employed to identify the semiquantitative elemental distribution analysis and the SEM image acquisition of as-prepared electrodes. Transmission electron microscope (JEM-F200, JEOL) was used to perform the microstructures. The prepared electrodes were fully grinding into powders and then highly dispersed in ethanol to satisfy the requirements of TEM. X-ray photoelectron spectroscopy analysis was performed by X-ray photoelectron spectroscopy (K-Alpha, Thermo Scientific).

### 2.4. Electrochemical measurement

In the three-electrode system, the graphite felt, Ag/AgCl electrode and graphite rod were employed as working electrode, reference electrode and counter electrode, respectively. Cyclic voltammetry measurements were completed in the solution containing 0.1 M VO<sup>2+</sup> + 3 M H<sub>2</sub>SO<sub>4</sub> by the electrochemical workstation (CHI 760E, Chenhua) at the scan rate of 5 mV s<sup>-1</sup>. The electrodes were measured in the voltage

range of 0.6–1.2 V (vs. Ag/AgCl) for VO<sup>2+</sup>/VO<sub>2</sub><sup>+</sup> reactions, and – 0.7 V to – 0.2 V (vs. Ag/AgCl) for V<sup>2+</sup>/V<sup>3+</sup> reactions. Electrochemical impedance spectroscopy measurements were performed with a frequency range from 10<sup>-2</sup> Hz to 10<sup>5</sup> Hz at the voltage of – 0.45 V for negative reactions and 0.9 V for positive reactions.

### 2.5. Flow-battery measurement

The single flow battery testing setup was mainly composed of porous electrodes separated by membranes, graphite plates with flow field, copper current collectors, and aluminum endplates. The membrane used in testing setup was Nafion NRE212. The GF, T-GF and G-NiCo<sub>2</sub>O<sub>4</sub>-GF with the geometrical area of 4 cm<sup>2</sup> were used as positive and negative electrodes. 20 mL solution with 1 M VO<sup>2+</sup> + 3 M H<sub>2</sub>SO<sub>4</sub> was employed as positive electrolyte, and 1 M V<sup>3+</sup> + 3 M H<sub>2</sub>SO<sub>4</sub> was negative electrolyte. The electrolyte is circled by peristaltic pump (WT600–2 J, Longer) with the flow rate of 46 mL min<sup>-1</sup>, in which the nitrogen gas was flowed through electrolyte with the flow rate of 10 mL min<sup>-1</sup> to avoid the detrimental side reactions with oxygen in air. The performances of flow batteries were tested by a battery test system (BT-G, Arbin) with the control of MITS PRO. For the battery charge-discharge measurement, the constant current tests (the operating current density ranged from 100 mA cm<sup>-2</sup> to 500 mA cm<sup>-2</sup>) with the cutoff voltage of 0.9 V and 1.65 V were conducted three times for every current density. As for the durability tests, the flow battery was operated at the current density of 200 mA cm<sup>-2</sup> over 200 cycles (nearly to 126 h).

### 2.6. Numerical methods

The average standard rate constants (*k*<sup>0</sup>) of T-GF electrode and G-NiCo<sub>2</sub>O<sub>4</sub>-GF electrode were accurately acquired from the tested CV curves (mentioned in session 2.4) by our recently reported intelligent CV analysis method [26]. Based on the achieved average *k*<sup>0</sup> of G-NiCo<sub>2</sub>O<sub>4</sub>-GF, setting *k*<sup>0</sup> of T-GF as minimum value, the linear function of standard rate constant for G-NiCo<sub>2</sub>O<sub>4</sub>-GF electrode can be deduced, substituting into the electrode mathematical model. Moreover, the maximum value of *k*<sup>0</sup> in G-NiCo<sub>2</sub>O<sub>4</sub>-GF electrode is directly adopted in the model to construct a uniform-enhanced electrode for comparison. The schematic of computational domain, source terms, and modeling parameters were shown in Fig. S1, Tab. S1, and Tab. S2, respectively. The details of multi-physics simulation method of flow battery were elaborated in the Supporting Information.

## 3. Results and discussion

As seen in Fig. 1, the basic idea is to fabricate the ordered-reaction electrode composed with gradient-distributed NiCo<sub>2</sub>O<sub>4</sub> nanorods. To complete this target, the first and foremost question is how to create a suitable reaction condition for the anisotropic nucleation. In this study, an ultra-low precursor concentration, that much lower than other studies reported [27], was adopted to construct an inadequate environment for nanorod generation. Furthermore, the porous carbon base was laid flat on the bottom of reactor to make the down side towards reactor wall while the up side exposed in solution, providing a differentiated condition for the gradient nucleation and growth of NiCo<sub>2</sub>O<sub>4</sub> nanorods. After the anisotropic-nucleation hydrothermal process, the G-NiCo<sub>2</sub>O<sub>4</sub>-GF electrode was prepared. As shown in Fig. 2a and b, two sides of G-NiCo<sub>2</sub>O<sub>4</sub>-GF electrode possessed distinctly differentiated apparent characteristics, in which the color of one side is light and another is nearly to T-GF. This is mainly attributed to the insufficient-reaction solvothermal method proposed in this research. Specifically speaking, the up side of electrode, which exposed more sites in the precursor solution, is light-colored, indicating abundant nanorods were generated. By contrast, the down side, with poor reaction environment in the bottom of reactor, is black-colored, suggesting scarcely any product on carbon fiber surface. To clear the interior structure and



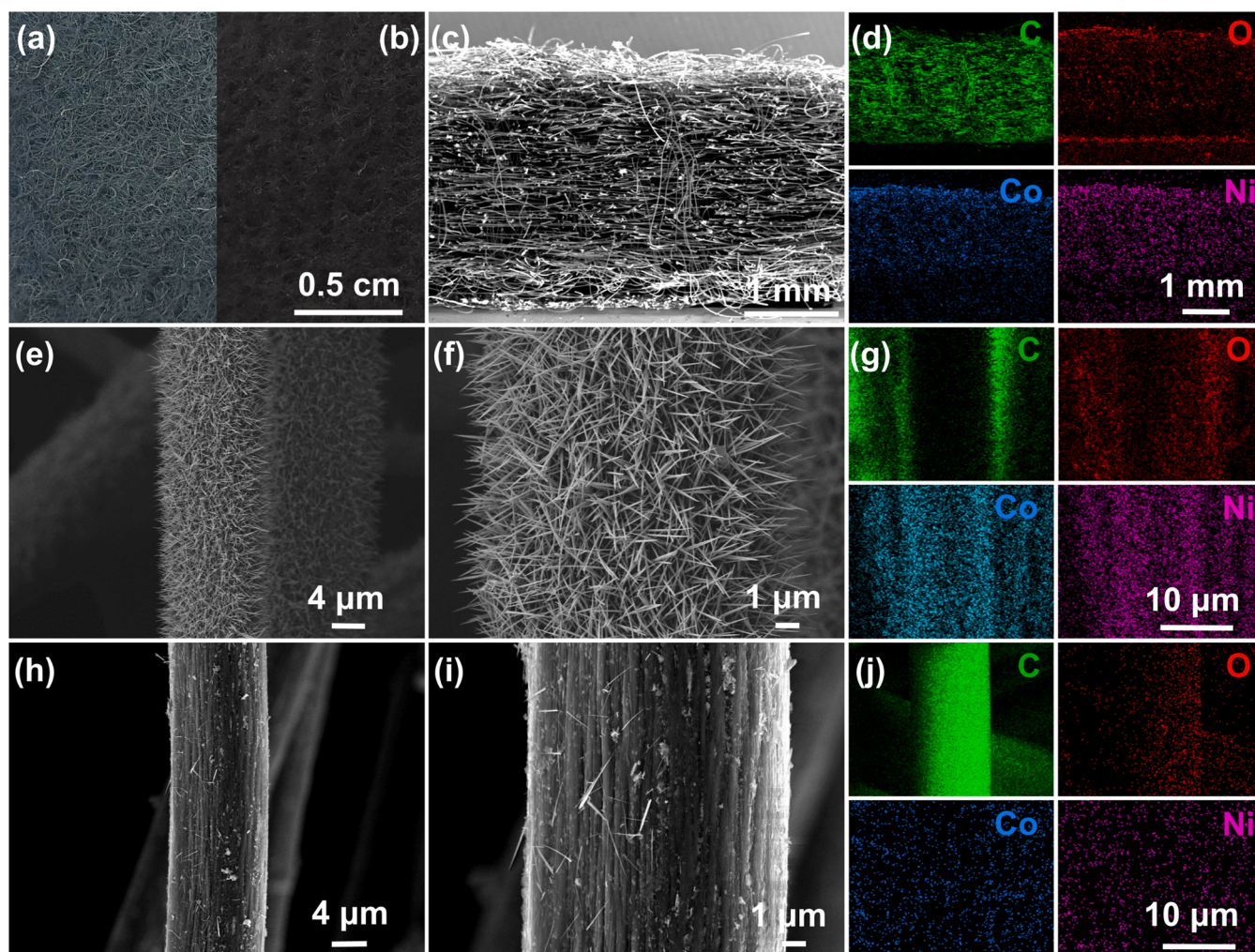


**Fig. 2.** Digital pictures of (a) the up side and (b) the down side of G-NiCo<sub>2</sub>O<sub>4</sub>-GF electrode. (c) SEM image and (d) EDS elemental mapping of the cross section of G-NiCo<sub>2</sub>O<sub>4</sub>-GF electrode. (e-f) SEM images and (g) EDS elemental mapping of the up side of G-NiCo<sub>2</sub>O<sub>4</sub>-GF electrode. (h-i) SEM images and (j) EDS elemental mapping of the down side of G-NiCo<sub>2</sub>O<sub>4</sub>-GF electrode.

the micro morphology of as-prepared electrode, the cross section in G-NiCo<sub>2</sub>O<sub>4</sub>-GF was further observed (Fig. 2c). As seen the elemental distributions of Fig. 2d, the distribution of carbon is even on the cross section, due to this GF-based electrode mainly consist of carbon fiber. The existences of oxygen, cobalt and nickel elements were also found in the electrode, signifying the generation of binary metal oxide compounded from Co and Ni. More noteworthy, the content of O element in G-NiCo<sub>2</sub>O<sub>4</sub>-GF electrode presented gradient distribution, increased from the down side to the up side, and the same is true of Co and Ni (Fig. 2d).

After observing the micro morphology, it can be clearly found that abundant and interlaced nanorods were generated on the carbon fiber surface in the up side of G-NiCo<sub>2</sub>O<sub>4</sub>-GF electrode (Figs. 2e and 2f). In the EDS mapping of Fig. 2g, the signals of O, Co and Ni were strong and the signal of C was blocked by the even-distribution nanorod. Significantly different with the up side, the carbon fiber surface of the down side was nearly smooth with few nanorod (Figs. 2h and 2i), in which the carbon signal is strong (Fig. 2j). Aiming at balancing the requirements between anisotropic transport properties and ordered reaction, the transport-reaction-matched gradient-distributed NiCo<sub>2</sub>O<sub>4</sub> nanorod composed electrode was constructed successfully, which can play critical roles for flow batteries (Fig. 1): i) in the weak-activity membrane side, abundant NiCo<sub>2</sub>O<sub>4</sub> nanorods with rich active sites were fabricated on carbon surface to locally enhance the activity; ii) in the high-rate flow field side, the smooth surface was remained to keep the structure stable against the

electrolyte flow; iii) in the whole electrode, the gradient-enhancement structure make charge distribution even and then lower the over-potential of the whole electrode.

The detailed microstructure characteristic of NiCo<sub>2</sub>O<sub>4</sub> nanorod was further confirmed by TEM. As seen in Fig. 3a, the wide of NiCo<sub>2</sub>O<sub>4</sub> nanorod is ~100 nm and the length is ~1 μm. The narrow structure can make this high-area nanorods as much as possibly form on the carbon fiber surface in the membrane side of electrode. High-resolution TEM (HRTEM) image in Fig. 3b displays a lattice distance of 0.30 nm for the (220) crystal plane of NiCo<sub>2</sub>O<sub>4</sub>. Moreover, the elemental mappings of oxygen, cobalt and nickel elements were uniformly dispersed on the nanorod, which was consistent with the conclusion of Fig. 2 (Fig. 3c-f).

The strong Co peaks and Ni peaks were observed in the survey X-ray photoelectron spectroscopy (XPS) spectra of the membrane side and the field side of G-NiCo<sub>2</sub>O<sub>4</sub>-GF electrode, as shown in Fig. 4a, which further confirmed the presence of the Co and Ni elements in the whole electrodes. More importantly, it was distinctly found that the Co peak and Ni peak displayed in the XPS spectra of membrane side are much stronger than that of field side, suggesting the nonuniform loading of NiCo<sub>2</sub>O<sub>4</sub> along the axial of this as-prepared electrode. In the high-resolution XPS spectra of Ni peak and Co peak in both sides, it was found the Co 2p peaks contain Co 2p<sub>3/2</sub>, Co 2p<sub>1/2</sub> characteristic peaks and two corresponding satellite (sat.) peaks, while Ni 2p peaks include Ni 2p<sub>3/2</sub>, Ni 2p<sub>1/2</sub> and two sat. peaks. To examine the chemical states of Co element



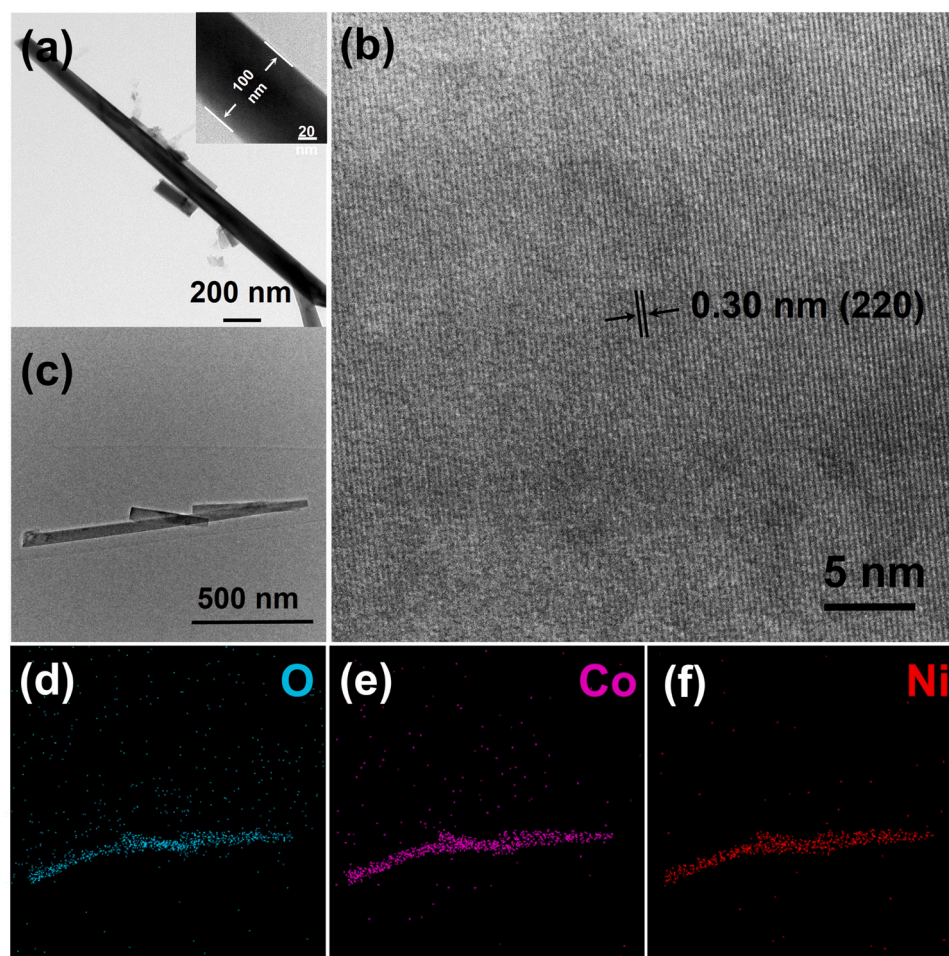


Fig. 3. (a-c) TEM images and (d-f) EDS elemental mapping of NiCo<sub>2</sub>O<sub>4</sub> nanorod.

at the electrode surfaces, the Co 2p<sub>3/2</sub> peaks were deconvoluted into Co<sup>2+</sup> (783.5 eV) and Co<sup>3+</sup> (782.1 eV) components, and the Co 2p<sub>1/2</sub> peaks were deconvoluted into Co<sup>2+</sup> (798.5 eV) and Co<sup>3+</sup> (792.1 eV) components (Fig. 4b). As for the Ni spectra, the peaks at 856.1 eV and 873.7 eV confirmed the existence of Ni<sup>2+</sup>, and the peaks at 857.7 eV and 875.3 eV were corresponded to Ni<sup>3+</sup> (Fig. 4b). It was found that the contents of Co<sup>2+</sup> and Co<sup>3+</sup> for the membrane side of G-NiCo<sub>2</sub>O<sub>4</sub>-GF electrode were obviously higher than those for the field side, so did the Ni<sup>2+</sup> and Ni<sup>3+</sup>, further indicating the generated gradient-distribution NiCo<sub>2</sub>O<sub>4</sub> nanorod on the carbon fiber surface.

The electrochemical activity of gradient-distribution NiCo<sub>2</sub>O<sub>4</sub> nanorod-composed GF electrode was accessed by cyclic voltammetry (CV) tests, as shown in Fig. 5a and b. Compared with GF and T-GF electrode, the G-NiCo<sub>2</sub>O<sub>4</sub>-GF showed enhanced performance in terms of peak separations, peak current ratios, and peak current densities. In CV tests, the membrane side of G-NiCo<sub>2</sub>O<sub>4</sub>-GF was set faced to the glassy carbon whilst the field side was exposed in the electrolyte. For the V<sup>2+</sup>/V<sup>3+</sup> redox reaction in Fig. 5a, the anodic peak current density of G-NiCo<sub>2</sub>O<sub>4</sub>-GF was 58.32 mA cm<sup>-2</sup> at the scan rate of 5 mV s<sup>-1</sup>, higher than that of T-GF (49.08 mA cm<sup>-2</sup>). And the pristine GF electrode, due to its sluggish graphite surface, exhibited almost nonexistent peak in CV curves. This was ascribed to the improved catalytic activity of the membrane side of G-NiCo<sub>2</sub>O<sub>4</sub>-GF, resulting in more accessible active sites than GF and T-GF. Such results also suggested that the active species in electrolyte could easily transported into the membrane side in practical flow battery, achieving the high utilization rate toward active sites. Moreover, the peak separation of G-NiCo<sub>2</sub>O<sub>4</sub>-GF (179 mV) was higher than that of T-GF (211 mV), while the peak current ratio of G-

NiCo<sub>2</sub>O<sub>4</sub>-GF (1.15) was closer to 1 than T-GF (1.26), signifying the reversibility of V<sup>2+</sup>/V<sup>3+</sup> redox reaction possessed an obvious enhancement on the G-NiCo<sub>2</sub>O<sub>4</sub>-GF surface. The enhanced activity of G-NiCo<sub>2</sub>O<sub>4</sub>-GF toward V<sup>2+</sup>/V<sup>3+</sup> redox reaction was attributed to the high-area nanorod with high-activity NiCo<sub>2</sub>O<sub>4</sub> surface. An excellent electrochemical performance of G-NiCo<sub>2</sub>O<sub>4</sub>-GF electrode was also found in the VO<sup>2+</sup>/VO<sub>2</sub><sup>+</sup> redox reaction as depicted in Fig. 5b. Specifically, the peak separation of G-NiCo<sub>2</sub>O<sub>4</sub>-GF was 180 mV at 5 mV s<sup>-1</sup>, lower than 258 mV of GF and 218 mV of T-GF. Additionally, the peak current ratio of G-NiCo<sub>2</sub>O<sub>4</sub>-GF was 1.17, while those of GF and T-GF were 1.48 and 1.27, further verifying the excellent activity of G-NiCo<sub>2</sub>O<sub>4</sub>-GF electrode. All these results signified that the NiCo<sub>2</sub>O<sub>4</sub> nanorod-decorated GF may appear exciting performance in the practical flow battery system.

The electrochemical performances of G-NiCo<sub>2</sub>O<sub>4</sub>-GF electrode were further analyzed by the EIS perturbation technique (Fig. 5c and d). The bulk resistances of these electrodes, correspond to the value of intersection of real axis and semicircle at high frequency, were found ranged from 1.6 to 1.7 Ω in both V<sup>2+</sup>/V<sup>3+</sup> and VO<sup>2+</sup>/VO<sub>2</sub><sup>+</sup> redox reactions, with the small differences of 0.1 Ω. The minor change of bulk resistances in G-NiCo<sub>2</sub>O<sub>4</sub>-GF electrode meant that the ohmic resistance in flow batteries with the nanorod decorated electrode would not increase. The charge transfer process was revealed by charge transfer resistance, which was the radius of semicircle in the at high frequency. Specifically, it is calculated that the charge transfer resistance of G-NiCo<sub>2</sub>O<sub>4</sub>-GF electrode was 0.88 Ω in the V<sup>2+</sup>/V<sup>3+</sup> redox reaction, lower than that of GF (1.65 Ω) and T-GF (58.41 Ω) (Fig. 5c). As for the VO<sup>2+</sup>/VO<sub>2</sub><sup>+</sup> redox reaction shown in Fig. 5d, the G-NiCo<sub>2</sub>O<sub>4</sub>-GF (2.57 Ω) also exhibited obviously lower charge transfer resistance with comparison of GF

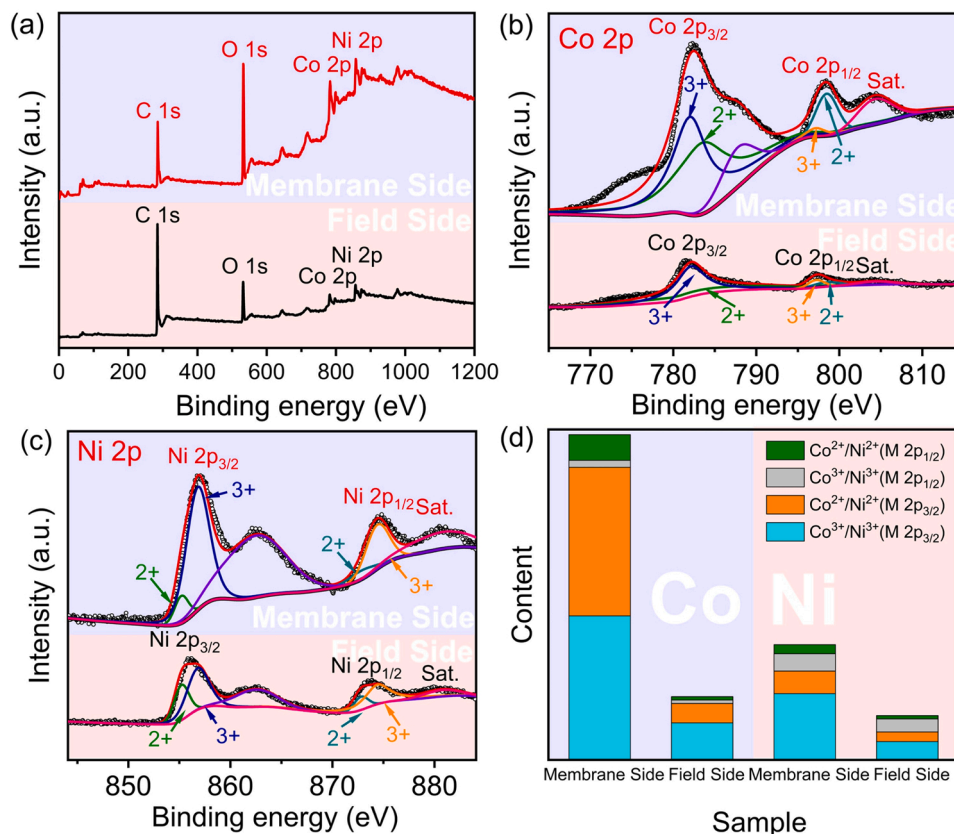


**Fig. 4.** (a) XPS spectra in the wide-range scan of G-NiCo<sub>2</sub>O<sub>4</sub>-GF electrode. XPS analysis and its fitting from the high resolution (b) Co 2p peak, and (c) Ni 2p peak of G-NiCo<sub>2</sub>O<sub>4</sub>-GF electrode. (d) Chemical composition ratio of G-NiCo<sub>2</sub>O<sub>4</sub>-GF electrode from Co 2p and Ni 2p spectra.

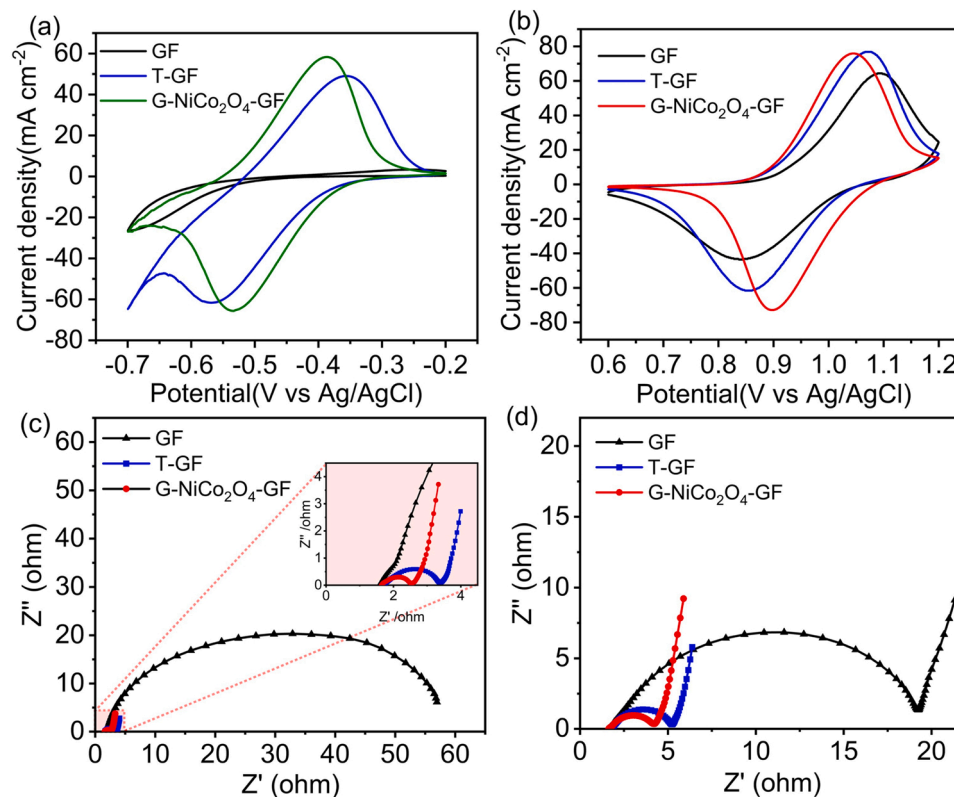


**Fig. 5.** CV curves of GF, T-GF and G-NiCo<sub>2</sub>O<sub>4</sub>-GF electrodes in the potential windows of (a) -0.7 to -0.2 V and (b) 0.6–1.2 V at the scan rate of 5 mV s<sup>-1</sup>. Nyquist plots of GF, T-GF and G-NiCo<sub>2</sub>O<sub>4</sub>-GF electrodes at the voltage of (c) -0.45 V and (d) 0.9 V.



(18.34  $\Omega$ ) and T-GF (3.51  $\Omega$ ) electrodes. These results are well consistent with the conclusion of previous CV measurement.

In order to clear the ordered reaction mechanism inside the G-NiCo<sub>2</sub>O<sub>4</sub>-GF electrode, the multi-physical model of VFB was constructed for simulating transport and reaction processes (Fig. 6a). From the achieved CV results in Fig. 5b, average standard rate constants of T-GF electrode and G-NiCo<sub>2</sub>O<sub>4</sub>-GF electrode were acquired by our recently reported intelligent CV analysis method [26]. Specifically, the average  $k^0$  of T-GF electrode is  $8.9 \cdot 10^{-7} \text{ m} \cdot \text{s}^{-1}$ , and the average  $k^0$  of G-NiCo<sub>2</sub>O<sub>4</sub>-GF electrode is  $18 \cdot 10^{-7} \text{ m} \cdot \text{s}^{-1}$ . Considering that the surface property of field side with minimal nanorods in G-NiCo<sub>2</sub>O<sub>4</sub>-GF is nearly to T-GF,  $k^0$  of T-GF can be set as a minimum value in the developed electrode. Based on the average  $k^0$ , the maximum value of  $27.1 \cdot 10^{-7} \text{ m} \cdot \text{s}^{-1}$  and linear function of  $k^0$  distribution in G-NiCo<sub>2</sub>O<sub>4</sub>-GF electrode were deduced, as shown in Fig. 6b. Plugging minimum  $k^0$ , maximum  $k^0$  and function of  $k^0$  into as-built model respectively, the transport and reaction characteristics of T-GF electrode ( $k^0 = 8.9 \cdot 10^{-7} \text{ m} \cdot \text{s}^{-1}$ ), uniformly-enhanced electrode ( $k^0 = 27.1 \cdot 10^{-7} \text{ m} \cdot \text{s}^{-1}$ ), and ordered-reaction G-NiCo<sub>2</sub>O<sub>4</sub>-GF electrode (gradient distribution of  $k^0$ ) were obtained by calculation. The value change of velocities (Fig. S5), concentrations (Fig. S6), overpotentials (Fig. S7) and local current densities (Figs. 6c and S8) in electrode midcourt line along thickness direction were achieved, in which the flow battery is in the charge process of 50 % SOC at 100 mA cm<sup>-2</sup>. Moreover, the distributions of concentrations (Fig. S2), velocities (Fig. S4) and local current densities (Fig. 6d-f) in various electrodes were obtained. It can be found that the concentration distribution of T-GF electrode is ununiform along the through-plane direction (Figs. S2 and S3), so as to the velocity distribution (Figs. S4 and S5). Due to the porous structure for mass transport is unchanged, same ununiform characteristics of concentration and velocity distributions were observed in uniformly-enhanced electrode and G-NiCo<sub>2</sub>O<sub>4</sub>-GF electrode (Fig. S6). A large difference of concentration and velocity was presented between membrane side (concentration is 465.19 mol m<sup>-3</sup>, velocity is 0.00035 m s<sup>-1</sup>) and field side (concentration is 499.95 mol m<sup>-3</sup>, velocity is 0.22232 m s<sup>-1</sup>), suggesting an ultra-ununiform mass transport process. As shown in Fig. 6c and d, the distribution of local current density was uneven in T-GF electrode, in which the local current density of the membrane side was 0.44 A cm<sup>-3</sup> and field side was 1.17 A cm<sup>-3</sup>. Thus, due to the ununiform transport characteristic, the redox reaction of active species was concentrated in

the field-side area of traditional T-GF electrode, while the membrane-side area is hardly to occur reactions. Although further enlarged standard rate constant in electrode can effectively decrease the overpotential (Fig. S7), the nonuniformity of current distribution was increased greatly (Fig. 6e). As seen, with increasing the standard rate constant of whole electrode from  $8.9 \cdot 10^{-7} \text{ m} \cdot \text{s}^{-1}$  up to the  $27.1 \cdot 10^{-7} \text{ m} \cdot \text{s}^{-1}$ , a maximum value in G-NiCo<sub>2</sub>O<sub>4</sub>-GF, the local current density difference between membrane side and field side is increased from 0.73 A cm<sup>-3</sup> up to 1.43 A cm<sup>-3</sup>, compounding the problems of polarization and durability in flow batteries. Fortunately, thanks to the gradient design of surface activity, the ordered-reaction G-NiCo<sub>2</sub>O<sub>4</sub>-GF electrode not only yielded the most uniform distribution of current density with a low difference of local current density along through-plane direction (Fig. 6c and f), nearly one third of the uniformly-enhanced electrode. Moreover, the G-NiCo<sub>2</sub>O<sub>4</sub>-GF electrode also possessed the lower overpotentials than T-GF electrode (Fig. S7). To quantify the uniformity on the three electrodes, specific values of local reaction current density to average reaction current density ( $j_{\text{ave}}$ ) towards these three electrodes were compared (Fig. S8). It can be found that the  $j/j_{\text{ave}}$  values of G-NiCo<sub>2</sub>O<sub>4</sub>-GF electrode are closer to 1 than T-GF and uniformly-enhanced electrode. The  $j/j_{\text{ave}}$  difference of G-NiCo<sub>2</sub>O<sub>4</sub>-GF electrode (0.73179) between membrane side and field side is much lower than that of T-GF electrode (1.07896) uniformly-enhanced electrode (2.11392), indicating the ordered reaction of the developed electrode enabled an excellent uniformity of current density. In the ordered reaction process, the field-side interface with low activity consumed less reactant and provided more sufficient electrolyte supply, whilst the membrane-side interface with high activity enhanced the local current density to uniformize its whole distribution. These simulation results indicate a more efficient and more stable flow battery can be built via the developed G-NiCo<sub>2</sub>O<sub>4</sub>-GF electrode.

Charge-discharge performance of vanadium flow battery is evaluated in a lab-made cell and compared with other electrodes. The charge-discharge curves of flow batteries assembled with GF, T-GF and G-NiCo<sub>2</sub>O<sub>4</sub>-GF electrodes at the current densities of 100 mA cm<sup>-2</sup> (Fig. 7a), 200 mA cm<sup>-2</sup> (Fig. 7b), 300 mA cm<sup>-2</sup> (Fig. 7c), 400 mA cm<sup>-2</sup> (Fig. 7d) and 500 mA cm<sup>-2</sup> (Fig. 7e) were recorded. As seen, the overpotentials of all flow batteries were observed increased with the current density, leading to the limited voltage window. Interestingly, the specific capacities of battery with G-NiCo<sub>2</sub>O<sub>4</sub>-GF electrode were close to

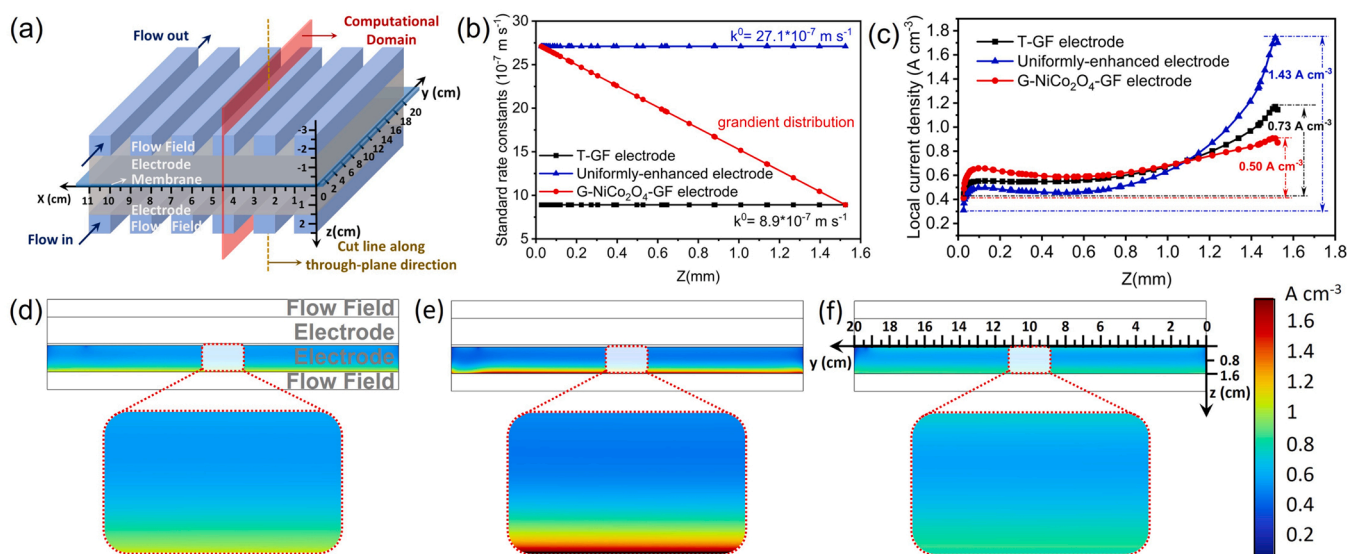


**Fig. 6.** (a) Flow segment model and computational domain of flow battery with parallel flow field (the  $z$ -length of flow field is 1 cm, the  $z$ -length of electrode is 1.6 cm, the  $z$ -length of membrane is 125  $\mu\text{m}$ ). The distributions of (b) standard rate constant, (c) local reaction current density along through-plane direction in battery charge process of 50 % SOC at 100 mA cm<sup>-2</sup>. The simulated current density distributions of VFBs with (d) T-GF electrode ( $k^0 = 8.9 \cdot 10^{-7} \text{ m} \cdot \text{s}^{-1}$ ), (e) uniformly-enhanced electrode ( $k^0 = 27.1 \cdot 10^{-7} \text{ m} \cdot \text{s}^{-1}$ ), and (f) ordered-reaction G-NiCo<sub>2</sub>O<sub>4</sub>-GF electrode.

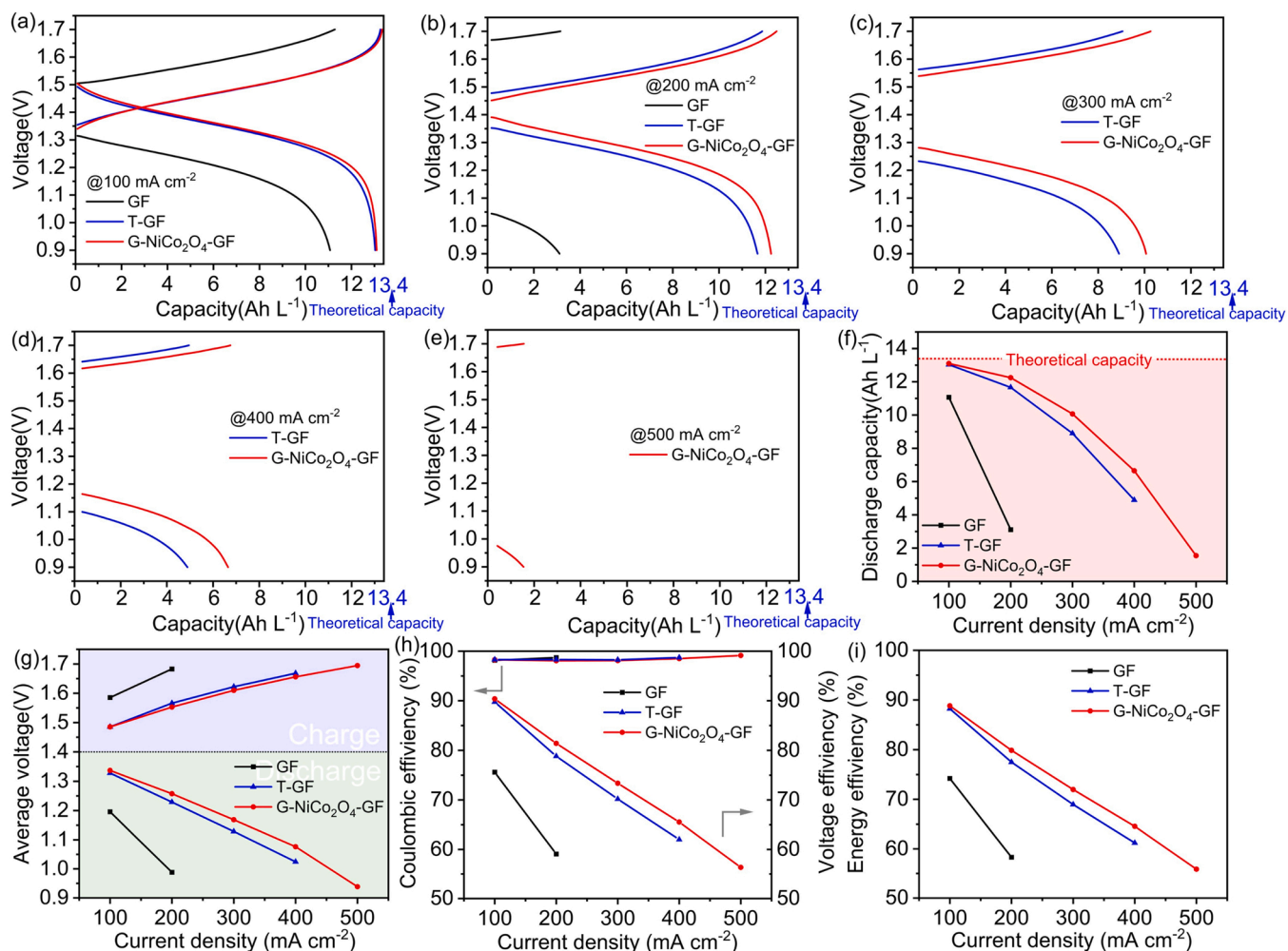


**Fig. 7.** Charge-discharge curves for VFBS with GF, T-GF and G-NiCo<sub>2</sub>O<sub>4</sub>-GF electrodes at current densities of (a) 100, (b) 200, (c) 300, (d) 400 and (e) 500 mA cm<sup>-2</sup>. (f) The discharge capacities of VFBS with GF, T-GF and G-NiCo<sub>2</sub>O<sub>4</sub>-GF electrodes from 100 to 500 mA cm<sup>-2</sup>. (g) The average charge/discharge voltages of VFBS with GF, T-GF and G-NiCo<sub>2</sub>O<sub>4</sub>-GF electrodes from 100 to 500 mA cm<sup>-2</sup>. (h) Coulombic and voltage efficiencies and (i) energy efficiency of VFBS with GF, T-GF and G-NiCo<sub>2</sub>O<sub>4</sub>-GF electrodes from 100 to 500 mA cm<sup>-2</sup>.

those of T-GF electrode at relatively low current density, yet significantly better than T-GF at relatively high current density more than 100 mA cm<sup>-2</sup>. These may attribute to that the gradient-decoration electrode locally enhanced the inactive area near the membrane to achieve the even charge distribution along the axial at high current densities, lowering the overpotential and then heightening the specific capacity. For instance, the battery with GF electrode showed the poor battery performance with a low discharge capacity of 3.11 Ah L<sup>-1</sup> at 200 mA cm<sup>-2</sup>, only 23.2 % of theoretical capacity, due to that the sluggish graphite surface cause the serious polarization losses in battery operation (Fig. 7b and f). By contrast, at the current density of 200 mA cm<sup>-2</sup>, the discharge capacity of batteries with T-GF and G-NiCo<sub>2</sub>O<sub>4</sub>-GF electrodes were up to 87.0 % and 91.4 % of theoretical capacity, respectively (Fig. 7b and f). As the increase of current densities, the advantages of G-NiCo<sub>2</sub>O<sub>4</sub>-GF electrode were gradually emerged. At the current density of 400 mA cm<sup>-2</sup>, G-NiCo<sub>2</sub>O<sub>4</sub>-GF electrode exhibited the discharge capacity of 6.65 Ah L<sup>-1</sup>, 36.0 % higher than that of T-GF electrode (Fig. 7d and f). Even at the current density as high as 500 mA cm<sup>-2</sup>, the battery assembled with G-NiCo<sub>2</sub>O<sub>4</sub>-GF was still capable of operating under the upper voltage limit of 1.65 V, while no curves were recorded for batteries with GF and T-GF electrodes (Fig. 7e and f). Thanks to that high-activity surface and gradient-enhancement structure lowered the overpotential, the G-NiCo<sub>2</sub>O<sub>4</sub>-GF electrode possessed higher discharge capacity and higher operation

current than traditional electrodes in flow batteries. Thus, the vanadium electrolyte, a significant portion of total cost in VRFBs, could be further efficiently utilized, realizing the cost reduction.

The similar trends were observed in the average charge/discharge voltages as shown in Fig. 7 g. The G-NiCo<sub>2</sub>O<sub>4</sub>-GF electrode, due to the improved overpotential in batteries, yielded the highest discharge voltage and the lowest charge voltage at the current densities from 100 to 500 mA cm<sup>-2</sup>. To clear the efficiencies of flow batteries with various of electrodes, the coulombic, voltage and energy efficiencies of flow batteries were further obtained (Fig. 7 h and i). The coulombic efficiencies of batteries with various electrodes at all current densities were higher than 98 %, indicating scarcely any adverse side reaction occurred in operation (Fig. 7 h). It can be also found that the voltage efficiencies were obviously decreased and the coulombic efficiencies were slightly increased with the current density, on account of the enlarged polarization and shortened operation time (Fig. 7 h). As expected, owing to that the voltage efficiency was closely related to the overpotential, the G-NiCo<sub>2</sub>O<sub>4</sub>-GF electrode showed higher voltage efficiencies in flow battery tests than GF and T-GF, and this difference obviously increased with current density (Fig. 7 h). Indeed, the voltage efficiency of G-NiCo<sub>2</sub>O<sub>4</sub>-GF electrode was only 0.69 % higher than that of T-GF electrode at a low current density of 100 mA cm<sup>-2</sup>, due to that the activation polarization has been lowered enough in both T-GF and G-NiCo<sub>2</sub>O<sub>4</sub>-GF electrodes. However, the problem of concentration polarization in even-



enhanced T-GF was further emerged at high current density. The ordered-reaction G-NiCo<sub>2</sub>O<sub>4</sub>-GF electrode enabled a 5 % higher voltage efficiency at 400 mA cm<sup>-2</sup> than T-GF and a high operation current density of 500 mA cm<sup>-2</sup>. Taking the demand of high current in flow battery application, it can be deemed that the advantages of this gradient-enhanced electrode will be further highlighted in the future commercialization. Owing to that energy efficiency was product of voltage efficiency and coulombic efficiency and coulombic efficiencies of all batteries were close, the energy efficiency was directly related to the voltage efficiency in this flow battery system. For instance, the energy efficacy of battery assembled with G-NiCo<sub>2</sub>O<sub>4</sub>-GF electrode was 88.81 % at 100 mA cm<sup>-2</sup> and 79.86 % at 200 mA cm<sup>-2</sup>, 20 % and 37 % higher than that of GF electrode, respectively. Even at the current densities as high as 500 mA cm<sup>-2</sup>, the battery with G-NiCo<sub>2</sub>O<sub>4</sub>-GF electrode reached the effective energy efficiency of 55.86 %, while the batteries with other electrodes could not normally operated under this condition. In summary, the modification of gradient-distribution nanorod on traditional electrode could lower overpotential and widen voltage window of all-vanadium flow battery, remarkably enhancing the energy efficiency and electrolyte utilization efficiency.

The stability of flow battery is crucial for the large-scale commercial application. In order to achieve the durability of this as-prepared electrode, the flow battery was cycling tested at the current density of 200 mA cm<sup>-2</sup> for more than 162 h. As depicted in Fig. 8, there was no obvious degradation of coulombic efficiency from 1st cycle to 200th cycle, owing to that scarcely any adverse side reaction occurred in the cycling tests. As for the energy efficiency, the G-NiCo<sub>2</sub>O<sub>4</sub>-GF electrode exhibited insignificant degradation of 0.046 % per cycle, suggesting superior stability of the gradient-distribution nanorod structure and activated NiCo<sub>2</sub>O<sub>4</sub> surface. Thus, in the lab scale, the gradient-distributed NiCo<sub>2</sub>O<sub>4</sub> nanorod-composed electrode could not merely offers enough active sites for redox reactions, but also possesses suitable gradient structure for mass transport, thus synergistically enhance the efficiency and stability of flow battery. Moreover, thanks for the simple one-step hydrothermal method, the large-area ordered-reaction electrode can also be fabricated with simple adjustments for the future large-scale engineering application. For example, the bottom area of the autoclave can be enlarged as requirement while its height keep a small value, so that the large-area electrode can be placed for mass production. Heater band can be set outside the autoclave to control the temperature and low-concentration precursor solution can lower the cost. Not just the hydrothermal method, various advanced technologies, such as inkjet printing and three-dimensional printing, can be adopted to mass and controllably product the ordered-reaction electrode for the future commercial application.

#### 4. Conclusion

To summarize, an ordered-reaction electrode composed with gradient-distributed NiCo<sub>2</sub>O<sub>4</sub> nanorod was proposed and developed as a high-performance electrode for flow batteries in this work. The uniquely developed electrode possesses the ordered reaction interface for matching mass transport properties: i) in the membrane side with low flow rate, the rich activated NiCo<sub>2</sub>O<sub>4</sub> nanorods enhance redox reaction and shorten proton transport distance; ii) in the field side with high flow rate, the smooth carbon-based framework stabilizes the mechanical structure against electrolyte scouring and offers pathway for mass transport; iii) in the whole electrode with non-uniform mass transport properties, the ordered redox reaction uniform the current distribution of electrode. The SEM and XPS measurements demonstrated a gradient-distributed characteristic of NiCo<sub>2</sub>O<sub>4</sub> nanorod in the developed electrode. In CV and EIS measurements, the G-NiCo<sub>2</sub>O<sub>4</sub>-GF electrode exhibited high electrochemical activity for vanadium ions redox reactions. The multi-physics simulated analysis demonstrated the synergic relationship of redox reaction and mass transport in the G-NiCo<sub>2</sub>O<sub>4</sub>-GF electrode. The VFB assembled with G-NiCo<sub>2</sub>O<sub>4</sub>-GF electrode exhibited

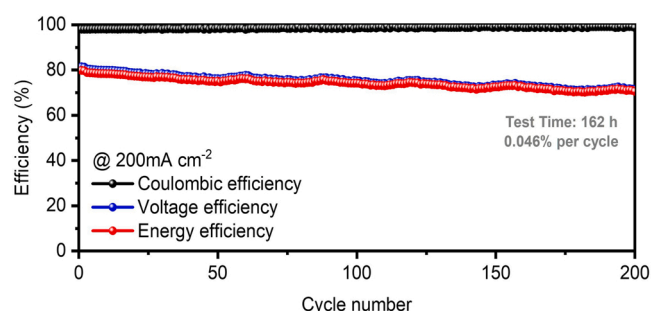


Fig. 8. Cycling performance of the VFB with G-NiCo<sub>2</sub>O<sub>4</sub>-GF electrode at the current density of 200 mA cm<sup>-2</sup>.

high efficiency, high operation current density, large discharge capacity and superior stability in the charge-discharge test. Moreover, thanks to the enhancement in local activity and conductivity of the G-NiCo<sub>2</sub>O<sub>4</sub>-GF electrode, the concentration overpotential was diminished, extending the potential windows for the charge and discharge processes. Therefore, the ordered-reaction electrode is greatly expected to be applied in flow battery technologies for its large-scale commercialization.

#### CRediT authorship contribution statement

**Rui Wang:** Methodology, Formal analysis, Investigation, Validation, Visualization, Data curation, Project administration, Funding acquisition, Supervision, Writing – original draft, Writing – review & editing. **Mingsheng Hao:** Software, Validation. **Chao He:** Investigation. **Zhengjun Tu:** Investigation. **Fazheng Chong:** Software, Validation. **Yinshi Li:** Conceptualization, Funding acquisition, Writing – review & editing.

#### Declaration of Competing Interest

The authors declare that they have no known competing financial interests or personal relationships that could have appeared to influence the work reported in this paper.

#### Data availability

The authors do not have permission to share data.

#### Acknowledgement

This work was supported by the National Natural Science Foundation of China (52176204, 22208259), the Natural Science Foundation of Shaanxi Province (2022JM-210), the Postdoctoral Science Foundation of China (2021M702571) and the Fundamental Research Funds for the Central Universities (xhj032021008-01, xhj032021008-04).

#### Appendix A. Supporting information

Supplementary data associated with this article can be found in the online version at doi:10.1016/j.apcatb.2023.122773.

#### References

- [1] R. Meys, A. Kätelhön, M. Bachmann, B. Winter, C. Zibunas, S. Suh, A. Bardow, Achieving net-zero greenhouse gas emission plastics by a circular carbon economy, *Science* 374 (2021) 71–76, <https://doi.org/10.1126/science.abg9853>.
- [2] J.P. Helveston, G. He, M.R. Davidson, Quantifying the cost savings of global solar photovoltaic supply chains, *Nature* 612 (2022) 83–87, <https://doi.org/10.1038/s41586-022-05316-6>.
- [3] X. Fu, G. Jiang, G. Wen, R. Gao, S. Li, M. Li, J. Zhu, Y. Zheng, Z. Li, Y. Hu, L. Yang, Z. Bai, A. Yu, Z. Chen, Densely accessible Fe-Nx active sites decorated mesoporous carbon-spheres for oxygen reduction towards high performance aluminum-air flow

- batteries, *Appl. Catal. B Environ.* 293 (2021), 120176, <https://doi.org/10.1016/j.apcatb.2021.120176>.
- [4] R. Jain, A.S. Lakhnot, K. Bhimani, S. Sharma, V. Mahajani, R.A. Panchal, M. Kamble, F. Han, C. Wang, N. Koratkar, Nanostructuring versus microstructuring in battery electrodes, *Nat. Rev. Mater.* 7 (2022) 736–746, <https://doi.org/10.1038/s41578-022-00454-9>.
  - [5] J. Sun, M.C. Wu, X.Z. Fan, Y.H. Wan, C.Y.H. Chao, T.S. Zhao, Aligned microfibers interweaved with highly porous carbon nanofibers: a novel electrode for high-power vanadium redox flow batteries, *Energy Storage Mater.* 43 (2021) 30–41, <https://doi.org/10.1016/j.ensm.2021.08.034>.
  - [6] W. Lu, X. Li, H. Zhang, The next generation vanadium flow batteries with high power density – a perspective, *Phys. Chem. Chem. Phys.* 20 (2018) 23–35, <https://doi.org/10.1039/C7CP07456E>.
  - [7] M. Yue, Z. Lv, Q. Zheng, X. Li, H. Zhang, Battery assembly optimization: tailoring the electrode compression ratio based on the polarization analysis in vanadium flow batteries, *Appl. Energy* 235 (2019) 495–508, <https://doi.org/10.1016/j.apenergy.2018.10.136>.
  - [8] D. Aaron, Z. Tang, A.B. Papandrew, T.A. Zawodzinski, Polarization curve analysis of all-vanadium redox flow batteries, *J. Appl. Electrochem.* 41 (2011) 1175–1182, <https://doi.org/10.1007/s10800-011-0335-7>.
  - [9] R. Wang, Y. Li, Carbon electrodes improving electrochemical activity and enhancing mass and charge transports in aqueous flow battery: status and perspective, *Energy Storage Mater.* 31 (2020) 230–251, <https://doi.org/10.1016/j.ensm.2020.06.012>.
  - [10] J. Sun, M. Wu, H. Jiang, X. Fan, T. Zhao, Advances in the design and fabrication of high-performance flow battery electrodes for renewable energy storage, *Adv. Appl. Energy* 2 (2021), 100016, <https://doi.org/10.1016/j.adapen.2021.100016>.
  - [11] A. Abbas, S. Abbas, A. Bhattarai, N.M. Latiff, N. Wai, A.N. Phan, T.M. Lim, Effect of electrode porosity on the charge transfer in vanadium redox flow battery, *J. Power Sources* 488 (2021), 229411, <https://doi.org/10.1016/j.jpowsour.2020.229411>.
  - [12] V.A. Beck, J.J. Wong, C.F. Jekel, D.A. Tortorelli, S.E. Baker, E.B. Duoss, M. A. Worsley, Computational design of microarchitected porous electrodes for redox flow batteries, *J. Power Sources* 512 (2021), 230453, <https://doi.org/10.1016/j.jpowsour.2021.230453>.
  - [13] B. Li, M. Gu, Z. Nie, Y. Shao, Q. Luo, X. Wei, X. Li, J. Xiao, C. Wang, V. Sprenkle, W. Wang, Bismuth nanoparticle decorating graphite felt as a high-performance electrode for an all-vanadium redox flow battery, *Nano Lett.* 13 (2013) 1330–1335, <https://doi.org/10.1021/nl400223v>.
  - [14] X. Zhang, X. Ye, S. Huang, X. Zhou, Promoting pore-level mass transport/reaction in flow batteries: Bi nanodot/vertically standing carbon nanosheet composites on carbon fibers, *ACS Appl. Mater. Interfaces* 13 (2021) 37111–37122, <https://doi.org/10.1021/acsami.1c08494>.
  - [15] D. You, J. Lou, X. Li, Y. Zhou, X. Sun, X. Wang, Investigation of advanced catalytic effect of Co<sub>3</sub>O<sub>4</sub> nanosheets modified carbon felts as vanadium flow battery electrodes, *J. Power Sources* 494 (2021), 229775, <https://doi.org/10.1016/j.jpowsour.2021.229775>.
  - [16] L. Wei, T.S. Zhao, L. Zeng, Y.K. Zeng, H.R. Jiang, Highly catalytic and stabilized titanium nitride nanowire array-decorated graphite felt electrodes for all vanadium redox flow batteries, *J. Power Sources* 341 (2017) 318–326, <https://doi.org/10.1016/j.jpowsour.2016.12.016>.
  - [17] S. Bellani, L. Najafi, M. Prato, R. Oropesa-Nuñez, B. Martín-García, L. Gagliani, E. Mantero, L. Marasco, G. Bianca, M.I. Zappia, C. Demirci, S. Olivotto, G. Mariucci, V. Pellegrini, M. Schiavetti, F. Bonaccorso, Graphene-based electrodes in a vanadium redox flow battery produced by rapid low-pressure combined gas plasma treatments, *Chem. Mater.* 33 (2021) 4106–4121, <https://doi.org/10.1021/acs.chemmater.1c00763>.
  - [18] J. Ye, C. Zheng, J. Liu, T. Sun, S. Yu, H. Li, In situ grown tungsten trioxide nanoparticles on graphene oxide nanosheet to regulate ion selectivity of membrane for high performance vanadium redox flow battery, *Adv. Funct. Mater.* 32 (2022), 2109427, <https://doi.org/10.1002/adfm.202109427>.
  - [19] F. Xing, T. Liu, Y. Yin, R. Bi, Q. Zhang, L. Yin, X. Li, Highly active hollow porous carbon spheres/graphite felt composite electrode for high power density vanadium flow batteries, *Adv. Funct. Mater.* 32 (2022), 2111267, <https://doi.org/10.1002/adfm.202111267>.
  - [20] L. Wei, C. Xiong, H.R. Jiang, X.Z. Fan, T.S. Zhao, Highly catalytic hollow Ti<sub>3</sub>C<sub>2</sub>Tx MXene spheres decorated graphite felt electrode for vanadium redox flow batteries, *Energy Storage Mater.* 25 (2020) 885–892.
  - [21] R.K. Sankaralingam, S. Seshadri, J. Sunarso, A.I. Bhatt, A. Kapoor, Overview of the factors affecting the performance of vanadium redox flow batteries, *J. Energy Storage* 41 (2021), 102857, <https://doi.org/10.1016/j.est.2021.102857>.
  - [22] X.L. Zhou, T.S. Zhao, L. An, Y.K. Zeng, X.H. Yan, A vanadium redox flow battery model incorporating the effect of ion concentrations on ion mobility, *Appl. Energy* 158 (2015) 157–166, <https://doi.org/10.1016/j.apenergy.2015.08.028>.
  - [23] Z. Huang, A. Mu, L. Wu, H. Wang, Vanadium redox flow batteries: flow field design and flow rate optimization, *J. Energy Storage* 45 (2022), 103526, <https://doi.org/10.1016/j.est.2021.103526>.
  - [24] H.R. Jiang, B.W. Zhang, J. Sun, X.Z. Fan, W. Shyy, T.S. Zhao, A gradient porous electrode with balanced transport properties and active surface areas for vanadium redox flow batteries, *J. Power Sources* 440 (2019), 227159, <https://doi.org/10.1016/j.jpowsour.2019.227159>.
  - [25] R. Wang, Y. Li, H. Liu, Y.-L. He, M. Hao, Sandwich-like multi-scale hierarchical porous carbon with a highly hydroxylated surface for flow batteries, *J. Mater. Chem. A* 9 (2021) 2345–2356, <https://doi.org/10.1039/D0TA10284A>.
  - [26] X. Wu, R. Wang, Y. Li, A thin-layer diffusion model-based intelligent cyclic voltammetry analysis method to capture electrochemical parameters in flow batteries, *Electrochim. Acta* 433 (2022), 141267, <https://doi.org/10.1016/j.electacta.2022.141267>.
  - [27] P. Cai, J. Zhao, X. Zhang, T. Zhang, G. Yin, S. Chen, C.-L. Dong, Y.-C. Huang, Y. Sun, D. Yang, B. Xing, Synergy between cobalt and nickel on NiCo<sub>2</sub>O<sub>4</sub> nanosheets promotes peroxymonosulfate activation for efficient norfloxacin degradation, *Appl. Catal. B Environ.* 306 (2022), 121091, <https://doi.org/10.1016/j.apcatb.2022.121091>.